CHAPTER

6

Volatile evolution and atmospheres of Trans-Neptunian objects

Leslie A. Young[a], *Felipe Braga-Ribas*[b], *Robert E. Johnson*[c]

[a]Southwest Research Institute, Boulder, CO, United States [b]Federal University of Technology, Paraná, Curitiba (UTFPR), PR, Brazil [c]Federal University of Technology, Paraná (UTFPR), Curitiba, PR, Brazil

6.1 Introduction

Several bodies in the Trans-Neptunian region have volatiles on their surfaces that have significant vapor pressures at the temperatures of the outer solar system: CH_4, N_2, and CO (with CO only detected on Pluto and Triton). When present, volatiles may raise significant atmospheres around these bodies at some times during the orbit of these Trans-Neptunian objects (TNOs). These would be vapor-pressure supported atmospheres, where the main atmospheric species exists also as a surface ice, and the surface pressure is a very sensitive function of that ice's temperature. Mars, Pluto, Triton, and, to some extent, Io are examples of vapor-pressure supported atmospheres. If, as expected, Eris, Makemake, and other TNOs are occasionally in this class at some time in their orbit, then vapor-pressure supported atmospheres would be more numerous than terrestrial atmospheres (Venus, Earth, and Titan), or gas giants. Rather than an oddity, vapor-pressure supported atmospheres may be the most common style of atmosphere in our solar system. These atmospheres are characterized by large seasonal pressure variations, and global transport of volatiles across the surface.

Vapor-pressure supported atmospheres may have been important in the evolution of the outer solar system. All the TNOs should have formed with some measure of these species, but not all TNOs have volatiles detected on their surface. The explanation is tied to the gaseous phase through atmospheric escape.

The atmospheres of Pluto and Triton have been extensively studied, by spacecraft, ground-based occultations and spectroscopy, and modeling. Great effort has been made to search for atmospheres around other TNOs. To date, only upper limits have been placed.

The Trans-Neptunian Solar System.
https://doi.org/10.1016/B978-0-12-816490-7.00006-0

6.2 Spectral evidence of N_2, CO, and CH_4 on the surfaces of TNOs

Methane ice has been reported or inferred on the surfaces Triton, Pluto, Eris, Makemake, Quaoar, Varuna, Sedna, and 2007 OR_{10}. CO and N_2 ices have been directly detected on Pluto and Triton. N_2 ice has been inferred from its effect on the CH_4-dominated spectra of Eris and Makemake, and possibly Quaoar and Sedna. We detail the evidence for the presence of such ices below and summarize it in Table 6.1. See de Bergh et al. (2013), Brown (2008, 2012), and Grasset et al. (2017) for earlier reviews, and Chapter 5 for more general discussion of the composition of TNO surfaces. Despite attempts to characterize surface compositions with photometric systems (Trujillo et al., 2011; Dalle Ore et al., 2015), spectral resolution of at least 500 seems to be needed for definitive detections of volatile ices, and we focus on spectral data in this chapter.

Triton: We consider Triton in the discussion of volatiles on TNOs, even though it is a moon of Neptune, because it is thought to be a captured TNO (McKinnon and Leith, 1995) and, more frivolously, its orbit clearly crosses that of Neptune. Its surface and atmospheric properties

TABLE 6.1 Volatile ices reported or suggested on TNOs.

Body	CH_4 ice	N_2 ice	CO ice
Triton	Multiple CH_4 bands directly detected	N_2 band directly detected. N_2-rich ice inferred from CH_4 band shifts	Multiple CO bands directly detected
(134340) Pluto	Multiple CH_4 bands directly detected	N_2 band directly detected. N_2-rich ice inferred from CH_4 band shifts	Multiple CO bands directly detected
(136199) Eris	Multiple CH_4 bands directly detected	N_2-rich ice inferred from CH_4 band shifts	No spectral evidence
(136472) Makemake	Multiple CH_4 bands directly detected	N_2-rich ice inferred from CH_4 band shifts	No spectral evidence
(50000) Quaoar	Multiple CH_4 bands possibly directly detected	N_2 band possibly directly detected. N_2-rich ice inferred from CH_4 band shifts	No spectral evidence
(225088) 2007 OR_{10}	CH_4 inferred by analogy with Quaoar	No spectral evidence	No spectral evidence
(90377) Sedna	Weak evidence longward of 2.2 μm; more work is needed	Weak evidence reported	No spectral evidence
(20000) Varuna	Weak evidence at 2.3 μm; more work is needed	No spectral evidence	No spectral evidence
(90482) Orcus	Possible absorption at 2.2 μm	No spectral evidence	No spectral evidence

are usefully compared to those of Pluto and other large TNOs. The volatiles N_2 and CH_4 were measured in Triton's atmosphere by Voyager during its 1989 flyby with its ultraviolet (UV) spectrometer (Broadfoot et al., 1989). Three relatively volatile ices, N_2, CH_4, and CO, and two nonvolatile ices, CO_2 and H_2O, were detected on Triton's surface from ground-based near-IR spectroscopy (Cruikshank et al., 1993, 2000). The spectral profile of the 2.15-μm N_2 absorption band is temperature dependent, and transitions from very broad for the higher-temperature hexagonal β-N_2 phase above 35.61 K to very narrow for the colder cubic α-N_2 phase. Noting this, Quirico et al. (1999) showed that the N_2 ice was in the warmer β phase on Triton. In addition, the spectrum of CH_4 ice diluted in N_2 is shifted toward shorter wavelengths with respect to pure CH_4 ice (Quirico and Schmitt, 1997; Protopapa et al., 2015). Therefore, it was concluded that solid CH_4 on Triton exists predominantly diluted in N_2 (Quirico et al., 1999), with subsequent observations suggesting the presence of some pure CH_4 ice (Merlin et al., 2018). These ices are not uniformly distributed across Triton's surface, as seen from the variation of its spectrum with subobserver longitude as the body rotates (Grundy and Young, 2004; Grundy et al., 2010; Holler et al., 2016). These studies suggest that the nonvolatiles H_2O and CO_2 may dominate the terrains nearest Triton's current summer pole, that the more volatile species, N_2 and CO, are colocated, and that the CH_4 distribution and mixing state may vary with depth and longitude. Furthermore, there is evidence for isolated areas of CH_4 diluted in N_2 that is too fine grained to allow direct detection of the inherently weak 2.15-μm N_2 band, where the presence of the N_2 is revealed only by its effect of shifting the CH_4 spectrum. Further clues to the distribution of Triton's ices comes from a long-time base of observations and Triton's changing aspect. Infrared spectra from 1986 to 1992—approaching Triton's summer solstice in 2000—show a dramatic decrease in Triton's 2.2–2.4 μm CH_4 band (Brown et al., 1995), while post-solstice spectra 2002–14 show a mild increase in CH_4 band depth (Holler et al., 2016), suggesting a combination of changing aspect and perhaps active volatile transport. Voyager flew no infrared spectrometer, and so it is likely that these speculations will remain unconfirmed until a mission to Neptune/Triton can fly an infrared spectrometer.

Pluto: Pluto's surface has been studied with disk-integrated ground-based spectra in the visible, near-infrared, and mid-infrared (see the review by Cruikshank et al., 2015) and at geologically relevant spatial scales by the LEISA-infrared spectrometer and MVIC color imager on NASA's New Horizons spacecraft (see Chapter 12). The N_2 ice on Pluto is concentrated in a large, deep, N_2-filled basin called Sputnik Planitia, near the equator and opposite Charon, in which some CO and CH_4 are diluted in solid solution with large grained or annealed β-N_2. N_2-rich ice of similar composition is also seen at mid-latitudes, 35–55°N (Protopapa et al., 2017; Schmitt et al., 2017). It is now understood that Pluto has more CH_4 than Triton overall. Areas of CH_4-rich ice was first inferred from ground-based spectra, and were mapped with the LEISA spectrometer to be predominately (i) at a northern cap, north of ~55°N, (ii) in a band from 20° to 35°N, and (iii) on the area named Tartarus Dorsae on the eastern terminator limb of the encounter hemisphere near 220–250°E, 10°S to 30°N.

Eris: The visible and near-infrared spectrum of Eris clearly shows strong CH_4 absorption features (Brown et al., 2005; see review by Brown, 2008 and analysis by Tegler et al., 2012). Absorption at 1.684 μm indicates pure CH_4 or CH_4-rich ice (Dumas et al., 2007), and the spectral shifts are much smaller than for either Triton or Pluto spectra. The depth, shape, and the precise wavelengths of the CH_4 features on Eris can be modeled to derive grain size, dilution state, and stratification of CH_4 ice, even without the direct detection of the N_2 feature (e.g., Merlin et al., 2009). The issue of stratification—that is, whether the CH_4 concentration state is constant or varying with depth—is particularly interesting because it relates to the evolution of Eris's ices over its 561-year orbit, which in turn is determined by the order in which different species freeze out onto the surface each orbit after perihelion. Different studies have disagreed on the stratification, variously concluding that the dilute CH_4 lies above pure CH_4 (Licandro et al., 2006a), below pure CH_4 (Abernathy et al., 2009), sandwiched between two layers of pure CH_4 (Merlin et al., 2009), or that the stoichiometry of CH_4:N_2 is constant with depth (Tegler et al., 2012). Clearly, better data and continued modeling is needed on this question. Eris's surface temperature is almost certainly below the α-β phase transition for N_2 (Sicardy et al., 2011), given its bright geometric albedo $p_V = 0.96$. Since the α-N_2 absorption feature is weaker and much narrower than that of β-N_2, it has eluded direct detection on Eris.

Makemake: Very strong CH_4 absorption is seen in the visible and infrared spectrum of Makemake with spectral shifts to shorter wavelengths, but with smaller shifts than are seen on Eris, Pluto, or Triton (Licandro et al., 2006b; Brown et al., 2007; Tegler et al., 2007, 2008; Lorenzi et al., 2015; Perna et al., 2017). This suggests that although some CH_4 is in solution with N_2, N_2 itself is not as prevalent on Makemake as on the previous three bodies. At visible wavelengths, Tegler et al. (2007) detected four absorption features between 0.54 and 0.62 μm that they attributed to CH_4, but ice-phase laboratory spectra of these features are lacking. The nonvolatile irradiation products of CH_4 are also seen on Makemake (Brown et al., 2015).

Quaoar: The spectrum of Quaoar is dominated by H_2O ice, analogous to H_2O-rich Charon. Jewitt and Luu (2004) interpreted absorption near 1.65 μm as crystalline water ice and absorption near 2.2 μm as ammonia hydrate, and reported no detected CH_4 absorption. Improved SNR at 2.2–2.4 μm strengthened the case for CH_4 in the spectrum (Schaller and Brown, 2007b), which, if real, was nevertheless subtle when superimposed on the significant H_2O absorption. Guilbert et al. (2009) claim a marginal detection (2 ± 2% deep) of the 1.724 μm feature due to CH_4 ice, which they say adds weight to the attribution of CH_4 ice for the 2.2 μm feature. Dalle Ore et al. (2009) model the near-IR spectrum plus photometry at 3.6 and 4.5 μm using CH_4 to explain both the 2.2 μm absorption and the mid-IR photometry, with no need for ammonia hydrate, and propose that N_2 ice in the β-phase may cover 20% of the surface, as seen by relatively subtle effects near 2.15 μm and by photometry at 3.6 and 4.5 μm. Barucci et al. (2015) investigate the 1.67-μm CH_4 band, and N_2 implied by the shifts in the 1.67-μm CH_4 band, but measuring this shift is complicated by the broad 1.65-μm crystalline H_2O band. In short, on Quaoar strong H_2O bands complicate the definitive detection and analysis of CH_4, and the derived presence of N_2 from CH_4 shifts.

2007 OR_{10}: The large TNO 2007 OR_{10} (Pál et al., 2016) shows an extremely red visible spectrum, and its near-IR spectrum shows water-ice absorption (Brown et al., 2011). 2007 OR_{10} shares both traits with Quaoar. This similarity with Quaoar is indirect evidence that CH_4 may also be present on 2007 OR_{10} (Brown et al., 2011), if one accepts both the equivalence of surface type and the evidence of CH_4 on Quaoar. Both Quaoar and 2007 OR_{10} are near the CH_4 retention line of Schaller and Brown (2007a) (see Section 6.4).

Sedna: Distant Sedna, currently at ~85 AU, has a spectrum that is difficult to interpret. Barucci et al. (2005) reported hints of a Triton-like spectrum with β-N_2 (an unexpected N_2

phase at Sedna's distance) and CH_4, from spectra with a spectral resolution of only 100 in the near-IR, while Trujillo et al. (2005) reported a featureless spectrum, from spectra at a binned resolution of 215 near 2.15 μm. Near-infrared spectra were analyzed in combination with Spitzer photometry at 3.6 and 4.5 μm (Barucci et al., 2010; Emery et al., 2007). No diagnostic CH_4 absorption bands were evident, but a decrease in albedo longward of 2.2 μm was interpreted as due to CH_4 and C_2H_6 (ethane), or possibly serpentine, and the addition of N_2 was also consistent with the Spitzer photometry (Barucci et al., 2010). The surface appears heterogeneous (Barucci et al., 2010).

Varuna: The spectrum of Varuna is in general well explained by various nonvolatiles, such as water ice, olivine, pyroxene, tholin, and amorphous carbon as a darkening agent. The strong CH_4 absorption bands at 1.67, 1.72, 1.8, or 2.21 μm are not detected in the current best spectra (Lorenzi et al., 2014), limiting the amount of CH_4 ice to less than 10% of the surface. Lorenzi et al. (2014) discuss how the addition of a small amount methane ice slightly improves the match to the data, but as their data have a spectral resolution of only 50, further work is critically needed to confirm or constrain CH_4 on Varuna.

Orcus: The water-dominated near-infrared spectrum of Orcus (de Bergh et al., 2005; Fornasier et al., 2004; Trujillo et al., 2005) has an absorption feature near 2.2 μm, compatible with absorption by CH_4, NH_3, or NH_4^+ (Barucci et al., 2008; Delsanti et al., 2010; Carry et al., 2011; DeMeo et al., 2010). Because of the lack of other CH_4 absorptions, specifically those near 1.67 and 1.72 μm, it is likely that CH_4 is not the main cause of the 2.2-μm absorption feature.

6.3 Volatile-supported atmospheres

For a TNO with little or no atmosphere, the equilibrium surface temperature, T_0, will depend on its rotation rate and thermal inertia (i.e., fast vs. slow rotator), latitude (λ), subsolar latitude (λ_{sol}), and time of day (e.g., hour angle of the Sun, h). The simplest approach is to assume thermal emission balances absorbed insolation, and that the atmosphere is nearly transparent, in which case the equilibrium surface temperature is

$$\epsilon\sigma T_0^4 = \overline{\mu(\lambda, \lambda_{sol}, h)} \left(\frac{S_{1AU}(1-A)}{\eta R^2} \right) \tag{6.1}$$

where ϵ is the emissivity, σ is the Stefan-Boltzmann constant, S_{1AU} is the normal solar insolation at 1 AU (1367 W m^{-2}), A is the bolometric Bond albedo, and R is the heliocentric distance in AU. $\overline{\mu(\lambda, \lambda_{sol}, h)}$ is the average cosine of the incidence angle for the problem at hand: For the subsolar temperature on a slow rotator, T_{ss}, $\overline{\mu} = 1$; for the equatorial latitude for fast rotator, $\overline{\mu} = 1/\pi$; for a single characteristic equilibrium temperature balancing the global average of the insolation, T_{eq}, $\overline{\mu} = 1/4$. η is the so-called "beaming factor" (e.g., Spencer, 1990; Harris, 1998; Müller et al., 2010; Lellouch et al., 2013), which can raise the temperature for a rough surface (or lower it for a body with high thermal inertia in some models of thermal emission). Many of the smaller TNOs have $A \approx 5\%$, while the largest TNOs have $A \approx 60\%$

–80% (Lellouch et al., 2013). Thus, the temperatures relevant for TNOs range from $T_{ss} \approx 70$ K for $\epsilon = 1$, $\eta = 1$, $A = 5\%$ at $R = 30$ AU down to $T_{eq} \approx 20$ K for $\epsilon = 1$, $\eta = 1$, $A = 80\%$ at 90 AU. Detached objects at R much greater 90 AU will have even colder temperatures. Eq. (6.1) ignores latent heat of sublimation and internal heat flux, and the conduction of heat into or from the subsurface is empirically included in the beaming factor.

The surface pressure of an atmosphere over a pure ice in thermodynamic equilibrium (the sublimation pressure, $p_s(T_0)$) is a function only of the ice temperature (Fray and Schmitt, 2009). Of the three volatiles seen in the outer solar system, N_2, CO, and CH_4, N_2 is by far the most volatile (Fig. 6.1). TNOs with volatiles show a mix of ices: CH_4 or CO diluted in N_2-rich ice; N_2 or CO diluted in CH_4-rich ice; or pure CH_4 ices. The mixtures present complicated surface-ice interaction, including lag deposits and the influence of CH_4-rich warm patches (see review by Trafton et al., 1998). Trafton (2015) and Tan and Kargel (2018) have more recent work on the mixtures, including the exciting conclusion that the CH_4 and N_2 partial pressures above a mixture of CH_4 saturated in N_2-rich ice plus N_2 saturated in CH_4 ice is independent of the bulk N_2:CH_4 ice ratio, but these have not been tested under laboratory conditions. Moreover, as seen in the compilation by Fray and Schmitt (2009), laboratory measurements for the pure ices only exist for temperatures above 54.78 K for CO and above 48.15 K for CH_4; and the only laboratory data below 35.4 K for N_2 were published in 1960 (Borovik et al., 1960).

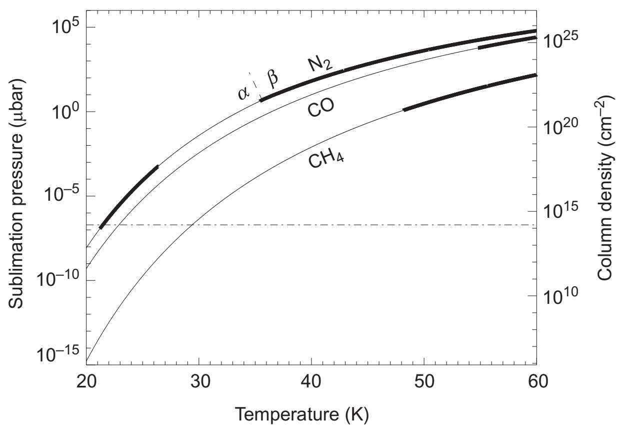

FIG. 6.1 Sublimation pressure (*left axis*) for N_2, CO, and CH_4 (Fray and Schmitt, 2009; FS09). The column density (*right axis*) is calculated for a body with bulk density ρ of 1.9 g cm^{-3} and a surface radius r of 500 km for N_2 or CO ($\mu = 28$) For a given pressure, the column density scales as $1/(\mu\, \rho\, r_0)$. Thus, the plotted column density (*right axis*) also applies for $\rho = 1.9$ g cm^{-3} and a surface radius r of 875 km for CH_4 ($\mu = 16$). *Thick lines* show the ranges of temperatures at or below 60 K from laboratory measurements included in FS09: For N_2, 21.20–26.40 K (Borovik et al., 1960), 35.40–59.17 K (Frels et al., 1974), and 54.78–61.70 K (Giauque and Clayton, 1933); for CO, 54.78–68.07 K (Shinoda, 1969); and for CH_4, 48.15–77.65 K (Tickner and Lossing, 1951) and 53.15–90.66 K (Armstrong et al., 1955). The α-β phase transition for N_2 is indicated (35.61 K). The *dot-dashed line* indicates the rough transition between ballistic and collisional atmospheres, for $\rho = 1.9$ g cm^{-3} and $r_0 = 500$ km.

The surface pressure is the weight of the column of gas, and so is closely related to the column density at the surface, N_0

$$p_s(T_0) \approx mg_0 N_0 \approx mg_0 H_0 n_0 \tag{6.2}$$

where m is the mass of molecule, and g_0 is surface gravity, given by $g_0 = GM/r_0^2$, where G is the gravitational constant, $M = \rho(4/3)\pi r_0^3$ is the TNO mass, ρ is the TNO bulk density, and r_0 is the surface radius. $H = kT_0/mg_0$ is the pressure scale height at the surface, k is Boltzmann's constant, and n_0 is the local number density at the surface. The relation is only approximate for small bodies, because gravity decreases with altitude.

For small column densities, the atmosphere can be described as a surface-bounded exobase, since if $N_0\,\sigma_{\mathrm{eff}} \ll 1$, where σ_{eff} is the effective collision cross-section, then an escaping molecule is not likely to suffer a collision on its way out. This condition is equivalent to a large Knudsen number, Kn, the ratio of the mean free path between collisions, $l_{\mathrm{mfp}} = 1/(n_0\,\sigma_{\mathrm{eff}})$, to a characteristic length scale. The scale in question depends on the problem at hand; taking the scale height for the length scale (Zhu et al., 2014), $Kn = 1$ is one classic definition of an exobase. At the surface:

$$Kn_0 = \frac{l_{\mathrm{mfp}}}{H_0} = \frac{1}{N_0 \sigma_{\mathrm{eff}}} \tag{6.3}$$

σ_{eff} is $\sqrt{2}$ times larger than the collisional cross-section, σ_{coll} (Johnson et al., 2015). Since $\sigma_{\mathrm{coll}} \approx 0.46 \times 10^{-14}$ for CH_4 (Atkins and de Paula, 2009) or $\sigma_{\mathrm{coll}} \approx 0.43 \times 10^{-14}$ for N_2 (Kaye and Laby, 1973), with some dependence on temperature, atmospheres with N_0 greater than $\sim 1.6 \times 10^{14}$ molecule cm^{-2} can be considered collisional. This is achieved for N_2 or CH_4 at extremely small surface pressures (Fig. 6.1), for example, $\sim 3 \times 10^{-8}$ μbar for CH_4 on a $\rho = 1.6\,\mathrm{g\,cm^{-3}}$, 100-km radius body, or $\sim 8 \times 10^{-7}$ μbar for N_2 on a $\rho = 2.5\,\mathrm{g\,cm^{-3}}$, 1000-km radius body. Extrapolating to these small pressures from the pressures measured in the lab is questionable, but application of the Fray and Schmitt (2005) compilations predicts that the transition to continuum atmospheres happens near temperatures of ~ 29 K for CH_4, and ~ 21 K for N_2, depending weakly on the TNO radius and density. For larger column densities, the atmosphere becomes opaque to UV radiation. This transition occurs for Ly-α at $N_0 \sim 10^{18}$ molecule cm^{-2} ($T_0 \sim 26$ K) for N_2 with 3% CH_4 gaseous molar mixing ratio, or $N_0 \sim 3 \times 10^{16}$ molecule cm^{-2} ($T_0 \sim 32$ K) for pure CH_4 (Johnson et al., 2015).

The Jeans parameter at the surface, or ratio of potential energy to thermal energy, is a measure of how tightly bound the atmosphere is, and is given by

$$\lambda = \frac{gm}{rkT} = \frac{U}{kT} = \frac{r}{H} = \frac{GMm}{r^2} \tag{6.4}$$

The Jeans parameter at the surface, λ_0, varies from ~ 0.1 (unbound) for CH_4 gas on 100-km radius objects at 70 K to ~ 100 (bound) for N_2 gas on 1000-km radius objects at 20 K. Although the composition surely varies from object to object, assuming each TNO has N_2 on its surface it can be seen from Fig. 6.2 that due to the large range of temperatures, the TNO atmospheres can have a large range of λ_0 and N_0, with implications for atmospheric escape, seasonal variation, and detectability.

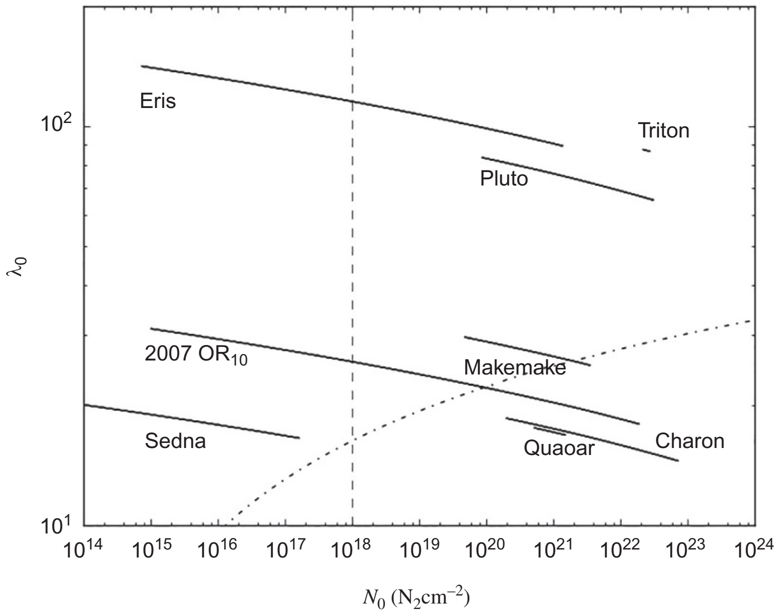

FIG. 6.2 Range of surface Jeans parameter, λ_0, versus total column density, N_0, over the orbits of a number of TNOs assuming an N_2 atmosphere (Johnson et al., 2015) using $\varepsilon = 0.8$ and $A = 0.67$, appropriate for an early TNO with a bright surface. For Makemake, 2007 OR_{10}, and Sedna we used $\rho = 1.8\,g\,cm^{-3}$. Sedna's values are shown only near perihelion as its aphelion ($N_0 \ll 10^{14}\,cm^{-2}$) is off-scale. *Dashed line*: $N_0 = 10^{18}\,N_2\,cm^{-2}$; to the right the CH_4 and N_2 components are sufficient so that escape is mainly driven by solar heating of the atmosphere. *Dotted-dashed line*: Surface-heating-induced escape rate is smaller than Jeans formula below this line (warmer surface or lower surface gravity) and greater above this line. *From Johnson, R.E., Oza, A., Young, L.A., Volkov, A.N., Schmidt, C., 2015. Volatile loss and classification of Kuiper belt objects. Astrophys. J. 809, 43. Reproduced by permission of the AAS.*

6.4 Expected volatile retention

In general, only the largest TNOs have had volatiles detected or suspected on their surfaces (Table 6.1). This is not merely an observational effect (i.e., because higher-quality spectra are more easily obtained on larger TNOs), but is linked to the escape of their initial inventory of volatiles (Schaller and Brown, 2007a; Levi and Podolak, 2009; Johnson et al., 2015). Volatile escape can be driven by heating of the surface by solar visible radiation and by absorption of solar radiation in the atmosphere. The relative importance of these processes depends on how tightly bound the atmosphere is, parameterized by the surface Jeans parameter λ_0, and its UV opacity, parameterized by its surface column density, N_0. Since the work of Schaller and Brown (2007a) and Levi and Podolak (2009), there has been progress in estimating the escape rate in the transition to the fluid regime for transparent atmospheres (Volkov et al., 2011a,b), and the role of atmospheric heating on escape (Johnson et al., 2013a,b, 2015), as well as new observations relating to initial volatile inventories (Glein and Waite, 2018) and the complexity of escape at Pluto (Gladstone and Young, 2019).

In order to provide a link between the presence of volatiles, the bulk properties, and the orbits of TNOs, Schaller and Brown (2007a) considered sublimation-induced escape directly from the TNO surface, and updated this work in Brown et al. (2011). Starting with the equilibrium surface temperature (e.g., Eq. 6.1 with $\overline{\mu} = 1/4$ and $\eta = 1$), they used the Jeans expression for escape from an exobase, evaluated at the conditions of the surface (subscripted here as SJ for surface Jeans):

$$\Phi_{SJ} = 4\pi r_0^2 n_0 \, (\bar{v}/4) \, (1 + \lambda_0) \exp(-\lambda_0) \tag{6.5}$$

where Φ is the total escape rate of volatiles in molecule s^{-1}, and $\bar{v} = \sqrt{8kT/\pi m}$ is the mean molecular speed. Using these expression for T_0 and Φ, they divided the TNOs into those that would likely keep their volatiles and those that likely lost their initial volatile inventory over the age of the solar system (Fig. 6.3).

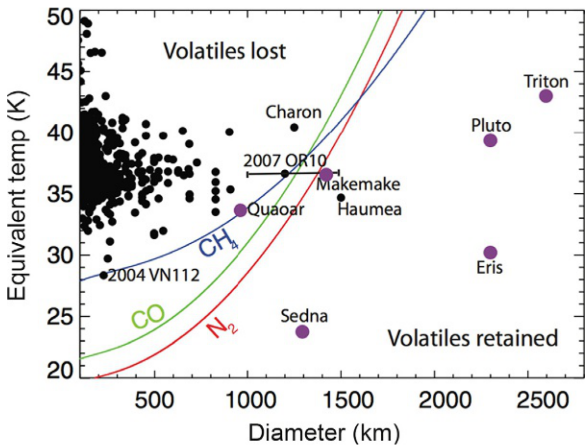

FIG. 6.3 Plot of volatile retention and loss in the Kuiper belt. Using the surface-Jeans formulation for atmospheric escape, objects to the left of the CH_4, CO, and N_2 lines lose surface volatiles over the age of the solar system. *From Brown, M.E., Burgasser, A.J., Fraser, W.C., 2011. The surface composition of large Kuiper belt object 2007 OR$_{10}$. Astrophys. J. 738, L26, updated from Schaller, E.L., Brown, M.E., 2007. Volatile loss and retention on Kuiper belt objects. Astrophys. J. 659, L61–L64. Reproduced by permission of the AAS.*

The surface-Jeans estimate of the escape rate is roughly accurate if the atmosphere is noncollisional, $N_0 \lesssim 10^{14}$ molecule cm^{-2} (Fig. 6.4), which holds for very distant TNOs. However, Eq. (6.5) is problematic, even for atmospheres that are transparent to solar heating. Levi and Podolak (2009) subsequently used a hydrodynamics model that transitioned to Jeans escape. Volkov et al. (2011a,b) used a molecular kinetic model, the direct simulation Monte Carlo (DSMC) method (Bird, 1994), to calculate the surface-heated escape rate, Φ_S, from a single-component atmosphere for a range of surface values of T_0 and N_0, and then expanded this range to very thick atmospheres by coupling iteratively to a fluid model in Johnson et al. (2015), thereby covering the full range of escape due to surface heating. Note that Volkov et al. (2011a,b) use the *radial* Knudsen number, scaling the mean free path by the surface radius, which is appropriate for small bodies with extended atmospheres (i.e., small λ_0). We denote that here as Kn_0^r (r for radial) and relate it to Eq. (6.3) through $Kn_0^r = l_{mfp}/r_0 = Kn_0/\lambda_0$. Johnson et al. (2015) fit an analytic expression to the numerical results of Volkov et al. (2011a,b) to find a correction to the surface-Jeans flux that depends on the surface values of the Knudsen number and Jeans parameter. We use Kn_0^r here to allow direct comparison with Volkov et al. (2011a,b) and Johnson et al. (2015).

$$\Phi_S = \Phi_{SJ}/[(Kn_0^r)^{0.09} + \lambda_0^{2.55} \exp(-\lambda_0)/(70Kn_0^r)] \tag{6.6}$$

For cold atmospheres and large bodies (high gravity), the escape rate driven only by the surface temperature is throttled for a bound atmosphere by the $\exp(-\lambda_0)$ term in Eq. (6.5), (Fig. 6.4). This can be overcome by direct absorption of solar radiation in the atmosphere. Assuming ~2%–3% CH_4 in the more volatile N_2 background gas, Johnson et al. (2015) calculated that the column of gas that is sufficient for the UV and EUV to be primarily absorbed in the atmosphere is $N_0 > N_C$, where $N_C \approx 10^{18}$ molecule cm^{-2} is the minimum column for UV absorption. Prior to the New Horizons encounter, models of Pluto's atmospheric loss coupled a fluid simulation to a DSMC molecular kinetic simulation (e.g., Erwin et al., 2013; Tucker et al., 2012) to describe the UV/EUV absorption versus depth as well as the escape from the exobase region. In their Pluto modeling, the simulated loss rate was matched reasonably well by the simple so-called energy-limited escape model, in which the gravitational energy lost by the escaping molecules is set equal to the heating produced by the absorbed UV radiation. The limits to the applicability of that model were explored in Johnson et al. (2013a,b) and subsequently applied to other TNOs (Johnson et al., 2015). Ly-α dominates the absorbed UV flux if CH_4 is optically thick. Since scattered interplanetary Ly-α and stellar flux contribute to the UV flux in the Trans-Neptunian region, the energy-limited flux falls off more slowly than R^2. Eq. (6.7) gives the expression adopted by Johnson et al. (2015) for the escape due to UV/EUV heating in the upper atmosphere, Φ_U, scaled to the detailed rate calculated for Pluto, Φ_P

$$\Phi_U = \Phi_P\,(\rho_P/\rho)\,[(30/R)^2 + 0.09] \tag{6.7}$$

where ρ_P and ρ are the density of Pluto and the TNO, R is the heliocentric distance in AU, and Φ_P is the escape rate at Pluto due to the direct solar UV flux. The second term in the brackets accounts for the so-called interplanetary UV flux (Gladstone, 1998) ignored in those papers but which becomes important at very large R. Johnson et al. (2015), based on Erwin et al. (2013) and Tucker et al. (2012), adopted $\rho_P = 2.05\,\mathrm{g\,cm^{-3}}$, and $\Phi_P = 120\,\mathrm{kg\,s^{-1}}/m_{N_2} = 2.6 \times 10^{27}\,N_2\,\mathrm{s^{-1}}$. Johnson et al. (2015) combined surface and upper atmospheric heating by restricting Φ_U to $N_0 > N_C$ and choosing the larger of Φ_S and Φ_U (Fig. 6.4). Fig. 6.4 only gives a rough guide for ranges in which global models of the two escape processes dominate. Johnson et al. (2015) integrated the combined atmospheric loss rates over the lifetime of individual TNOs (Table 2 in Johnson et al., 2015, which did not include Orcus and Varuna). Besides Charon, which has likely lost its initial volatiles, they concluded that for the objects studied only Makemake, Quaoar, and 2007 OR_{10} likely lost a large fraction of their volatiles, primarily due to short wavelength absorption in their upper atmospheres, while Pluto, Triton, and Sedna had retained most of theirs. While similar conclusions were reached by Schaller and Brown (2007a), the fraction of volatiles retained by Pluto, Triton, and Sedna differed.

The picture created by these simulations has been altered by two recent spacecraft measurements. One is our more recent understanding of Pluto's atmosphere based on the New Horizons observations (Gladstone and Young, 2019). Prior to the flyby, the expected escape rate was ~[0.4−4] × $10^{27}\,N_2\,\mathrm{s^{-1}}$ (Zhu et al., 2014), consistent with energy-limited escape. The escape rate that is derived from the observed density and temperature profile is much

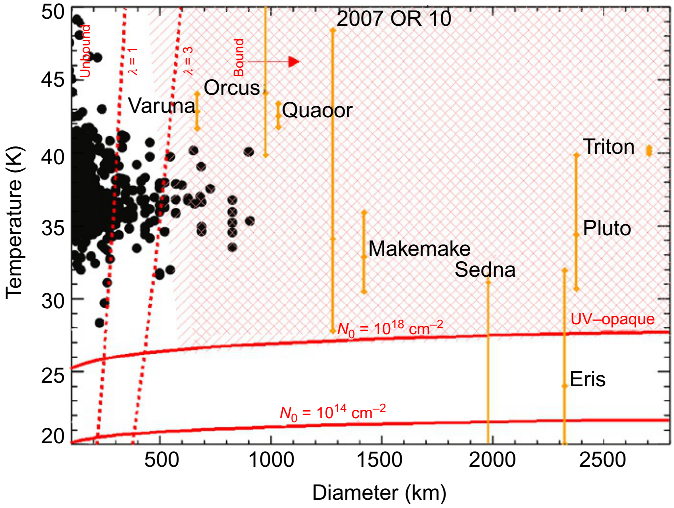

FIG. 6.4 Diagram of escape regimes. *Yellow*: The nine bodies in Table 6.1 have been plotted: *Solid vertical lines* show the variation in the average equilibrium temperatures between aphelion and perihelion (Eq. 6.1), using diameters and albedos from the *tnosarecool* database (i.e., updated from Brown et al., 2011 and Johnson et al., 2015). *Black*: Diameters and temperatures for other bodies are taken from the retention plot of Brown et al. (2011), as plotted in Fig. 6.3. *Solid red*: Lines of constant column density at the surface for two critical values: for $N_0 = 10^{14}\,\mathrm{cm}^{-3}$ defining the classical surface-bounded exobase, and $N_0 = 10^{18}\,\mathrm{cm}^{-3}$ for an N_2 atmosphere with 3% CH_4 to be opaque to Ly-α. *Dashed red*: Lines of constant Jeans parameter for two critical values dividing the unbound and bound atmosphere (Volkov et al., 2011b). *Hashed red*: Atmospheric heating dominates the loss rate in the shaded region for (adapted from the shaded regions in Fig. 3 of Johnson et al., 2015) $A = 0.1$ (*single hash*) and $A = 0.67$ (*cross-hatched*). Outside the hashed area, the surface-heated escape rate for warm, small bodies is much smaller than the surface-Jeans estimate, but the surface-heated escape rate for cold, large bodies is slightly larger than the surface-Jeans estimate (cf. *dot-dashed line* in Fig. 6.1).

lower: (3–7) $\times$ $10^{22}\,N_2\,s^{-1}$ and (4–8) $\times$ $10^{25}\,CH_4\,s^{-1}$ (Young et al., 2018). Applying these new observations has been confounded by the fact that the principal cooling agent in Pluto's upper atmosphere, which also compressed the extent of Pluto's atmosphere, is still uncertain (Gladstone and Young, 2019). Pluto's current escape rate must be better understood before volatile loss can be calculated for Pluto at other epochs, or for other bodies. The second is new constraints on the initial inventory of volatiles. While Schaller and Brown (2007a) and Johnson et al. (2015) used an N_2 to H_2O mass ratio of 2%, Glein and Waite (2018) use the mixing ratio of N_2 measured in the coma of 67P (Rubin et al., 2015) to derive an N_2 to H_2O mass ratio of only [0.7–6] $\times$ 10^{-4}.

6.5 Variation of atmospheres over an orbit

Because the sublimation pressures depend exponentially on the temperatures of the volatile ices, the gases surrounding volatile-bearing TNOs vary with heliocentric distance and subsolar latitude, and possibly time of day and latitude. This was initially modeled for Triton and

Pluto (see reviews by Spencer et al., 1997; Yelle et al., 1995). Since those reviews, trends of increasing atmospheric pressure for both Triton and Pluto were observed using the technique of stellar occultation, with an increase by factors of 2 and 3, respectively (Elliot et al., 1998, 2000a,b, 2003a; Olkin et al., 1997, 2015; Meza et al., 2019; see Section 6.6). The new time base of atmospheric observations and the New Horizons flyby of Pluto inspired new models of seasonal variation (e.g., Young, 2012, 2013, 2017; Hansen et al., 2015; Olkin et al., 2015), including general circulation models (e.g., Forget et al., 2017) and evolution of atmospheres on the timescale of millions of years (e.g., Bertrand and Forget, 2016; Bertrand et al., 2018).

When N_2 was discovered on the surface of Eris, authors speculated that volatiles on TNOs, especially N_2, could raise temporary atmospheres near perihelion (e.g., Dumas et al., 2007). This was generalized in Stern and Trafton (2008), and applied numerically to the known or suspected volatile-bearing TNOs by Young and McKinnon (2013). When thinking about atmospheres on TNOs, it is useful to distinguish three types: global, collisional, and ballistic. For global sublimation-supported atmospheres, such as Mars or current-day Pluto and Triton, volatiles sublime from areas of higher insolation, and recondense on areas of lower insolation, transporting latent heat as well as mass (Trafton, 1984; Ingersoll, 1990; also see reviews by Spencer et al., 1997; Yelle et al., 1995; Stern and Trafton, 2008). As long as the volatiles can be effectively transported, the surface pressures and the volatile ice temperatures will be nearly constant across the surface. Sublimation winds transport mass from latitudes of high insolation to low insolation. Trafton (1984) showed that pressures stay within 10% across the surface if the sublimation winds (v) are less than 7.2% of the sound speed (v_s). The sublimation wind speeds can be found by conservation of mass; the mass per time crossing a given latitude equals the integral of the net deposition from that latitude to the pole. The wind speeds depend on the subsolar latitude (Trafton, 1984), if we consider diurnally averaged insolation; higher wind speeds are needed to transport volatiles pole to pole (high subsolar latitudes) than equator to pole (low subsolar latitudes). For an "ice ball" uniformly covered in volatiles, the maximum sublimation wind speed, v, can be expressed as

$$vmN_0 = \xi Sr/L \tag{6.8}$$

where $S = S_{1AU}(1-A)/R^2 = 4\varepsilon\sigma T_{avg}^4$ is the absorbed normal insolation, and L is the latent heat of sublimation, in energy per mass. ξ in Eq. (6.8) is a numerical factor accounting for the subsolar latitude, λ_{Sun}. We calculated ξ numerically, following the prescription of Young (1993). From these calculations, ξ is well approximated by a cubic expression

$$\xi(\lambda_{Sun}) \approx 0.044 + 0.148(\lambda_{Sun}/90°) + 0.4012(\lambda_{Sun}/90°)^2 - 0.296(\lambda_{Sun}/90°)^3 \tag{6.9}$$

For a 400–1400-km radius body uniformly covered with CH_4 ice to have a global atmosphere, the pressure needs to be greater than ~17–295 nbar for polar illumination (3.1×10^{19} to 1.6×10^{20} cm^{-2}, 41.0–45.6 K; Fig. 6.5), or 1.9–33 nbar for equatorial illumination (3.6×10^{18} to 1.8×10^{19} cm^{-2}, 38.1–42.0 K). For N_2, the pressures are similar, so the temperatures are lower: 14–244 nbar for polar (1.5×10^{19} to 7.4×10^{19} cm^{-2}, 29.1–31.9 K) or 2–28 nbar for equatorial (1.8×10^{18} to 68.5×10^{18} cm^{-2}, 27.2–29.7 K). N_0 increases slightly faster than r because both S and N_0 increase with temperature; p_0 increases even faster, slightly faster than r^2, because of its dependence on g_0 (Eq. 6.2).

The temperatures in Fig. 6.5 are highly simplified. Seasonal thermal inertia can be important, even at the long timescales in the outer solar system. More significantly, bodies are unlikely to be uniformly covered in volatiles. For example, much of the N_2 on Pluto is located in the basin known as Sputnik Planitia (Moore et al., 2016), and Triton's N_2 may be perennially confined to the southern hemisphere (Moore and Spencer, 1990).

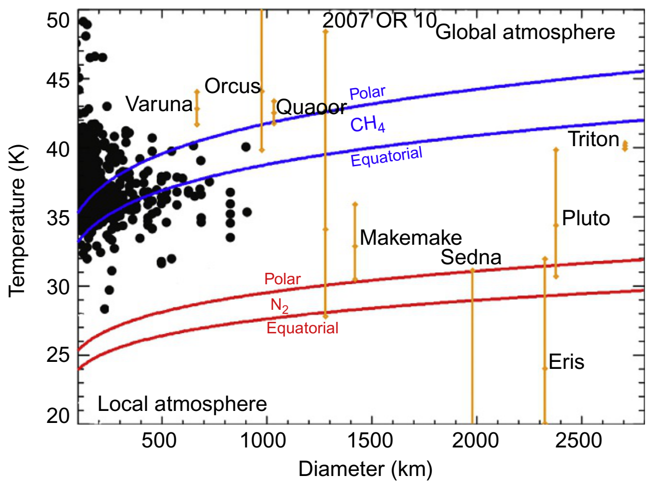

FIG. 6.5 In a global atmosphere, pressures are high enough so that the sublimation winds can keep surface pressures and volatile ice temperatures nearly uniform over the globe. Minimum temperatures for a global atmosphere are plotted, assuming a surface uniformly covered with CH_4 ice (*blue*) or N_2 ice (*red*), for two extreme subsolar latitudes. Several bodies would have global atmospheres at some portion of their orbit if covered with N_2 ice (as reported on Triton, Pluto, Eris, Makemake, and possibly Quaoar). A much smaller number of bodies would have global atmospheres at some portion of their orbit if covered with only CH_4 ice (as reported possibly on Varuna, Orcus, Quaoar, Sedna, and 2007 OR_{10}). Thermal inertia and nonuniform volatile ice coverage can change the range of temperatures actually achieved. Temperatures and diameters are as in Fig. 6.4.

Nonglobal atmospheres will vary with location and time of day, but may still be collisional, if the column density is greater than $\sim 10^{14}$ cm^{-2} for either N_2 or CH_4. Io is a classic example of a local atmosphere that is collisional around the subsolar point, and demonstrates some of the processes that are active in even these thin atmospheres. Atmospheric chemistry can occur even in these local, tenuous atmospheres (Wong and Smyth, 2000). Supersonic winds certainly flow and transport volatiles, even if they are not effective at equalizing pressures and temperatures (e.g., Walker et al., 2012). Recently, Hofgartner et al. (2018) used the Ingersoll et al. (1985) meteorological model developed for Io study the transport of N_2 on Eris at aphelion, when it is a local, collisional atmosphere, and found significant transport of N_2 ice. Even for more tenuous "surface-bounded exospheres," the loss of volatiles can modify landforms (see review by Mangold, 2011). For example, sublimation erosion may lead to the narrow divides between craters on Hyperion (Howard et al., 2012) or redeposition on the crater rims on Callisto, where the convex summits see less of the warm surface than do concave crater interiors, and are therefore local cold traps (Howard and Moore, 2008).

6.6 Detections of or limits on atmospheres by stellar occultation

The technique of stellar occultation is one of the most powerful ways to search for atmospheres around these bodies. While infrared absorption or radio emission have detected low column densities of CO and CH_4 on Triton (Lellouch et al., 2010) or CO and HCN on Pluto (Lellouch et al., 2017), these are bright targets. Stellar occultations depend on the brightness of the occulted star, and also study the target's size, shape, and the presence or nature of rings or jets (see Chapter 19; Elliot and Olkin, 1996; Elliot and Kern, 2003; Santos-Sanz et al., 2016). In an occultation, the starlight is refracted through a bending angle that increases in magnitude roughly in proportion to the line-of-sight column density (N_{los}). This leads to differential refraction, or a divergence of the refracted rays (cf. Elliot and Olkin, 1996), which dims the occulted starlight according to the scale height H and the column density. Some insight can be gained (Fig. 6.6) from the approximate, analytic expression for the relative stellar flux (e.g., Elliot and Young, 1992)

$$\varphi \approx \left|1 - \theta \frac{\Delta}{H}\right|^{-1} \left|1 + \theta \frac{\Delta}{r}\right|^{-1} e^{-\sigma_{\text{ext}} N_{\text{los}}} \tag{6.10}$$

where θ is the bending angle, given by $\theta \approx -\nu_{\text{STP}} N_{\text{los}} / n_{\text{STP}} H$, ν_{STP} is the refractivity at standard temperature and pressure (2.9×10^{-4} and 4.4×10^{-4} for N_2 and CH_4 at 0.7 µm), n_{STP} is Loschmidt's constant (2.6868×10^{19} cm^{-3}), and Δ is the target-observer distance. As before, r is the radius (distance from target center) and H is the atmospheric scale height. N_{los} is the line-of-sight column density (molecule per area), which is larger than N, the vertical

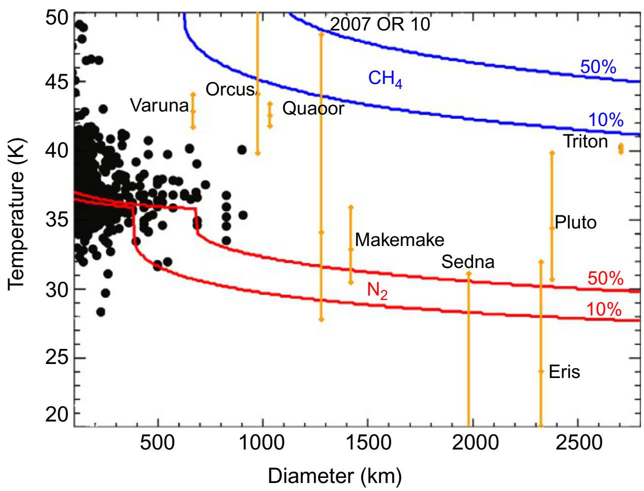

FIG. 6.6 Detectability of TNO atmospheres by ground-based stellar occultation, under the assumption that the atmosphere is isothermal, and both atmosphere and surface are at the plotted temperature. The *blue* (CH_4) and *red* (N_2) detectability limits are for 50% or 10% drop in stellar flux for a surface-grazing ray. Near 35 K for N_2 and 50 K for CH_4, the surface-grazing ray causes a central flash (Eq. 6.10, second term), which leads to a discontinuity in the derived limits; the plotted limits are somewhat conservative near this discontinuity Temperatures and diameters are as in Fig. 6.4.

column density, by the unitless factor $\sqrt{2\pi\lambda}$ (e.g., 8–25 for $\lambda \approx$ 10–100). σ_{ext} is the extinction cross-section (area per molecule). The first term represents the decrease due to the divergence (defocusing) of rays perpendicular to the limb, and halves the starlight when $\theta\Delta \approx -H$. The second term represents the increase due to refocusing parallel to the limb, leading to a "central flash" near the center of the shadow. The final term represents extinction, which becomes important when $N_{\text{los}} \approx 1/\sigma_{\text{ext}}$ (e.g., $N_{\text{los}} \approx 10^{26}$ molecule cm^{-2} for Rayleigh scattering at visible wavelengths, or $N_{\text{los}} \approx 10^{17}$ molecule cm^{-2} for typical cross-sections in the extreme UV). Refraction is typically dominant over extinction for Earth-based stellar occultations of TNOs, and extinction dominates for spacecraft UV occultations.

Light curves from model atmospheres can be calculated analytically for some idealized atmospheres (e.g., isothermal or $T \propto r^{\beta}$, $\beta \ll 1$; Elliot and Young, 1992). However, the presence of CH_4 or its by-products (including photochemical haze) can heat up the atmosphere by 10 s of K (Yelle and Lunine, 1989; Zhang et al., 2017). For more complex atmospheres, synthetic light curves are calculated under the assumption of geometric optics/ray tracing (Sicardy et al., 1999 and references therein) or wave optics/Fresnel diffraction (French and Gierasch, 1976). Standard model fitting can then be used to extract the geometric edge and the refractivity of the atmosphere at the surface. For high-quality data (as has been obtained for Pluto and Triton), light curves can be inverted to extract temperature, pressure, and number-density profiles (e.g., Elliot et al., 2003b). Derived surface pressures (or upper limits) from occultation light curves can be compared to the sublimation pressures for the atmospheric molecules under consideration, as expected from its surface equilibrium temperature (Fray and Schmitt, 2009).

Synthetic light curves versus shadow radius are plotted in Fig. 6.7 for an example TNO with an N_2 or CH_4dominated atmosphere (see caption for model details). Very thin atmospheres (10–100 s of nanobar, or $\sim 10^{19}$–10^{20} molecule cm^{-2}) cause only a small drop of flux very close to the surface, requiring very high signal-to-noise ratio for detection. Denser atmospheres (a few μbar, or $\sim 10^{20}$ molecule cm^{-2}) cause a gradual drop in the star flux at a significant distance from the object's surface, so they will be easier to detect. For denser atmospheres, the ray that grazes the TNO surface is refracted inward significantly toward smaller shadow radii (bent by 94–112 km for 1 μbar CH_4 or N_2 atmospheres). For the 10 μbar curve in Fig. 6.7, the surface-grazing ray is refracted past the shadow center. The bottom flux never reaches zero and much of the light curve is the sum of the near and far limb contributions. In the example plotted, the limb-grazing ray is bent by 900–1180 km for a CH_4 or N_2 atmospheres, leading to the discontinuities seen at ±400 or ±680 km for the CH_4- or the N_2-dominated atmospheres. When the star crosses the center of the object as seen from Earth, it causes a prominent central flash for the 10 μbar atmosphere, as the atmosphere acts as a lens, converging the starlight from all parts of the atmosphere to the observer.

Stellar occultations by Pluto, Charon, and Triton have been observed since the 1980s.

Pluto: A single-chord occultation from 1985 was observed under extremely difficult circumstances (Brosch, 1995). The definitive discovery of Pluto's atmosphere was from the 1988 stellar occultation (Hubbard et al., 1988; Millis et al., 1993). Observations in 2002 showed a doubling of the pressure since 1988 (Sicardy et al., 2003; Elliot et al., 2003a). Many high-quality observations since have revealed the continued changes in Pluto's atmosphere, its thermal structure, and waves (Young et al., 2008; Toigo et al., 2010; Sicardy et al., 2016; Dias-Oliveira et al., 2015; Pasachoff et al., 2017; Meza et al., 2019). The New Horizons radio and solar occultations

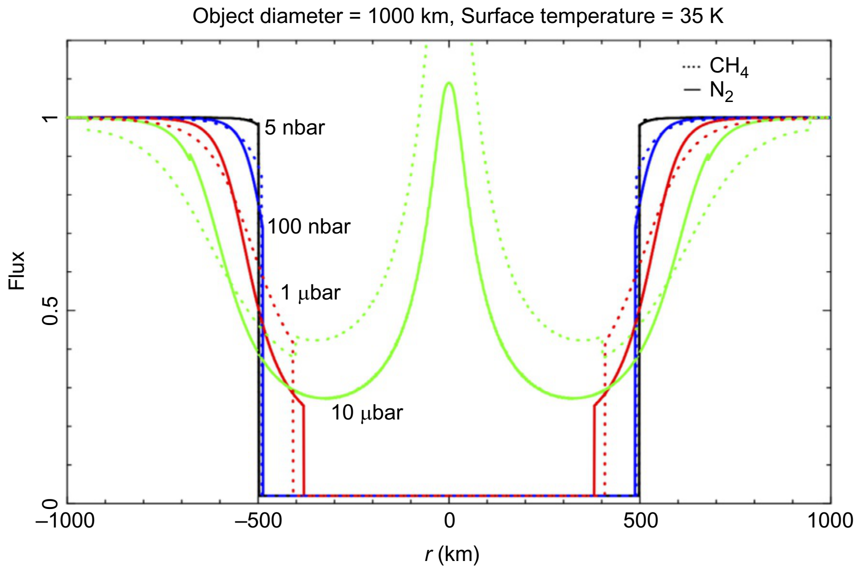

FIG. 6.7 Synthetic light curve models of normalized stellar flux versus shadow radius for an object with r_0 = 500 km, density 1.9 g cm^{-3}, Δ = 40 AU, with a surface temperature of T_0 = 35 K and a 5 K km^{-1} gradient to a 100 K upper atmosphere. *Continuous lines* are for an N_2-dominated atmosphere with surface pressures and column densities of p_0 = 5 nbar, N_0 = 4.0 × 10^{18} molecule cm^{-2} (*black*); 100 nbar, 8.1 × 10^{19} molecule cm^{-2} (*blue*); 1 μbar, 8.1 × 10^{20} molecule cm^{-2} (*red*), and 10 μbar, 8.1 × 10^{21} molecule cm^{-2} (*green*). *Dashed lines* are for a CH_4-dominated atmosphere with surface pressures and column densities of 0.005 μbar, 7.1 × 10^{18} molecule cm^{-2} (*black*); 0.1 μbar, 1.4 × 10^{20} molecule cm^{-2} (*blue*); 1 μbar, 1.4 × 10^{21} molecule cm^{-2} (*red*); and 10 μbar, 1.4 × 10^{22} molecule cm^{-2} (*green*).

revealed N_2 in vapor-pressure equilibrium with the N_2-rich ice, an overabundance of gaseous CH_4 possibly explained by CH_4-rich patches, hazes, and photochemical products, a cold upper atmosphere, and an atmospheric escape rate that was dominated by CH_4 and was much smaller than expected (see Chapter 12; Gladstone and Young, 2019).

Triton: Triton, like Pluto, was visited by a spacecraft, and has had several high-quality occultations, notably the November 4, 1997 Triton occultation observed from HST (Elliot et al., 1998). Occultations in the 1990s show a doubling of surface pressure on decadal timescales compared to the 1989 flyby by Voyager 2 (Elliot et al., 1998, 2000a,b; Young et al., 2002). An occultation from 2017 suggests that the increase has peaked (Oliveira et al., 2018; Person et al., 2018).

Charon: Prior to the New Horizons flyby, limits on Charon's atmosphere were set to be <50 nbar (1σ) from stellar occultation (Gulbis et al., 2006), and the New Horizons UV occultation set limits of <1.4 pbar (Stern et al., 2017).

Since 2009, stellar occultations have been successfully used to study other TNOs, and the search for an atmospheric signature was carried for a few of them. Most of the largest bodies have already observed during a stellar occultation event and no atmosphere around a TNO has been found so far (other than Pluto and ex-TNO Triton). Upper limits on the presence of putative atmospheres were obtained and they are summarized in Table 6.2.

TABLE 6.2 Results on atmospheres from stellar occultations.

Name	Equivalent radius (km)	Surface pressure	References
Triton	1350	3–11 μbar	Elliot et al. (2000b)
Pluto	1188	4–12.7 μbar	Sicardy et al. (2016)
Eris	1163	<1 nbar[a]	Sicardy et al. (2011)
Haumea	816	<10 nbar[a]	Ortiz et al. (2017)
Makemake	715	<12 nbar[a]	Ortiz et al. (2012)
Charon	606	<1.4 nbar[a]	Stern et al. (2017)
Quaoar	555	<21 nbar[a]	Braga-Ribas et al. (2013)
Sedna	445	Inconclusive	Braga-Ribas et al. (2014b)

[a] $1-\sigma$ *upper limits.*

Eris: A stellar occultation of a $V = 17.1$ star by Eris was observed on November 6, 2010 (Sicardy et al., 2011). Eris, the second-biggest TNO after Pluto, was at 95.7 AU and had a surface temperature estimated at 30 K. With methane and nitrogen detected on its surface, it was a good candidate to have retained volatiles. The occultation allowed a constraint on the presence of an isothermal N_2 atmosphere to an upper limit of 1 nbar at the surface, with similar limits for CH_4 and argon. The occultation revealed that Eris is one of the brightest objects of the solar system, with a geometric albedo of $p_v = 0.96$ (+0.09/−0.04), which may be caused by a collapsed atmosphere, as discussed earlier. As the subsolar temperature of Eris can reach 35 K, the authors mentioned that a local subsolar atmosphere of N_2 may exist, but it would freeze to undetectable values at the limb. It is suggested that, due to the eccentric orbit of Eris, when it approaches its perihelion at 37.8 AU, it may develop a global atmosphere of 2 μbar.

Haumea: An observation of a stellar occultation by Haumea on February 21, 2017 revealed that it also possesses a dense ring of 70 km in width (Ortiz et al., 2017), making it the second small solar system object, after (10199) Chariklo (Braga-Ribas et al., 2014a), known to have a ring. Upper limits (1σ) were obtained for the atmosphere of $p_0 < 10$ nbar (CH_4) or $p_0 < 3$ nbar (N_2). This is consistent with the lack of spectral evidence of CH_4 or N_2 on Haumea's surface. Haumea's ring, two moons, and the Haumea dynamical family suggest that volatiles were lost via a disruptive collision (e.g., Schaller and Brown, 2007b).

Makemake: A Makemake occultation of a $V = 18.5$ star on April 23, 2011 was detected from seven telescopes in Chile (Ortiz et al., 2012). The preferred solution for the projected shape is an ellipsoid with axes of 1430 ± 9 and 1502 ± 45 km. Constraining the shape to a circular cross-section gives a radius of 1430 ± 9 km, and is also consistent with the observations. The preferred (elliptical) solution gives a geometric albedo at V of $p_V = 0.77 \pm 0.03$. This is a bright albedo, and is consistent with surface freshening by a periodic atmosphere. No global atmosphere was detected, with limits on a global atmosphere of <12 nbar (1σ). This is somewhat surprising, as Makemake was a candidate for a global atmosphere, especially given the report of N_2 ice from CH_4 band shifts. The conclusion is that Makemake has lost almost all of its N_2 gas, or that the atmosphere near the limb has frozen to undetectable values (e.g., for a pole-on orientation or a slow rotation/low thermal inertia). Ortiz et al. (2012) also modeled the effect of a local atmosphere on the occultation light curves, motivated by some points close to centrality with an elevated flux a few σ above the noise, and placed loose limits on a local atmosphere of $p_0 < 30\ \mu$bar.

Quaoar: A large TNO ($r_0 = 550$ km) with CH_4 reported on its surface, Quaoar was a candidate to possess a thin atmosphere. It was observed crossing in front of a star on May 4, 2011, from which upper limits on the presence of an atmosphere were derived (Braga-Ribas et al., 2013). Being at a distance of 42.4 AU, with a geometric albedo of 0.109, a surface equilibrium temperature of 40 K is expected. Considering a CH_4 dominant atmosphere, reaching 102 K above 10 km from the surface, an upper limit of $p_0 < 21$ nbar (1σ) was obtained. As N_2 would have a vapor pressure of 66–176 μbar at 40–42 K, the data rule out this scenario.

Smaller TNOS: Additional TNOs have been observed during stellar occultations, and no clear signals of any atmosphere were detected. For these events, there are no published upper limits, because the decrease in stellar flux was abrupt (rather than dimming by atmospheric refraction), and the data did not have high enough quality (cadence or signal-to-noise ratio) for any constraints on a thin atmosphere. The larger bodies (equivalent radii $r_0 > 200$ km) so probed include Varuna ($r_0 = 568$ km; Sicardy et al., 2010), 2003 VS_2 ($r_0 = 274$ km; Benedetti-Rossi et al., 2019), 2002 TC_{302} ($r_0 = 499$ km; Santos-Sanz, 2017), 2003 AZ_{84} ($r_0 = 382$ km; Dias-Oliveira et al., 2017), and 2007 UK_{126} ($r_0 = 319$ km; Benedetti-Rossi et al., 2016).

6.7 Future research

The earlier discussion suggests some critical directions for future research.

Surface compositions:

- The spectra of Pluto and Triton change on the timescale of decades, and are related to both changing viewing geometry and possibly real changes in the volatile distribution or physical state of volatile ices (e.g., grain size). The changing compositions of Triton (visual magnitude $V = 13.4$) and Pluto ($V = 14.2$) can and should continue to be tracked with moderate ground-based telescopes, to decouple these effects.
- For other large TNOs, new understanding of the surface stratification of CH_4 and N_2 on Eris ($V = 18.7$) needs higher spectral resolution and SNR than previous spectra, as does the confirmation of or constraints on CH_4 on Quaoar ($V = 18.7$), 2007 OR_{10} ($V = 21.3$), Sedna ($V = 20.8$), Varuna ($V = 20.1$), and Orcus ($V = 19.2$). Some progress is likely to come from the new generation of infrared detectors (e.g., NIRES on Keck, or NIHTS on DCT). JWST's spectral sensitivity from 1 to 5 μm will be very powerful for measuring the volatiles and other species on the surfaces of these and other TNOs (Parker et al., 2016; see Chapters 5, 12, 18, and 19). Both the Thirty Meter Telescope and the European Extremely Large Telescope have planned near-infrared integral field spectrometers as first light instruments, and their various white papers emphasize how they will revolutionize TNO spectroscopy.

Laboratory work:

- The vapor pressures of CO and CH_4 should be measured at TNO temperatures of 20–40 K, and the vapor pressure of N_2 should be remeasured in a modern lab. Also, recent work on

the vapor pressures of mixed volatile ices (Trafton, 2015; Tan and Kargel, 2018) should be tested under laboratory conditions.
- Measurements of the spectrum of CH_4 ice in the visible, both pure and in solution with N_2, are needed for quantitative analysis of Makemake's CH_4 features 0.54–0.62 μm.

Atmospheric retention and escape:

- The most critical work is a better model of why the escape rate at Pluto in 2015 ($\sim 5 \times 10^{22}$ N_2 s^{-1} and $\sim 6 \times 10^{25}$ CH_4 s^{-1}) is so much lower than the energy-limited rate expected preencounter ($\sim 2 \times 10^{27}$ N_2 s^{-1}), and how that model can be applied to Pluto at other seasons, and to other TNOs.
- Current DSMC work on volatile retention only models a single species, but the observed mixed surfaces with both N_2 and CH_4 suggest new DSMC work with multiple species. Similarly, local atmospheres (e.g., dome-like atmospheres over the subsolar point) can be more completely modeled.

Seasonal transport:

- Models such as Hofgartner et al. (2018) can be used to investigate the transition between global and collisional atmospheres.

Atmospheric searches:

- Higher SNR occultations with higher cadence can help the sensitivity, and can help break ambiguity in the cases of suspected local atmospheres. Accurate star positions are now given by the Gaia catalog, but ephemeris errors are nearly always much greater than the object's apparent angular size. Astrometric positions are needed for the targeted TNOs. One source of positions can be the big and deep surveys like the Large Synoptic Sky Survey that is expected to begin observations in 2022, and will help to update TNOs ephemerides and so improve stellar occultation predictions (Camargo et al., 2018).

Acknowledgments

Leslie Young was supported in part by the NASA OPR Grant NNX14AO45G "Connecting Present and Past KBOs." Felipe Braga Ribas acknowledges CNPq Grant 309578/2017-5 and the funding from the European Research Council under the European Communities H2020 (2014–20/ERC Grant Agreement No. 669416 "LUCKY STAR"). Apurva Oza was invaluable in the calculations behind the work in Fig. 6.4. Thanks to Bryan Holler for discussions on Section 6.2, and Larry Trafton for discussion relating to the requirements for a global atmosphere. Mike Brown graciously allowed the reproduction of his figure from Brown et al. (2011), which provided some level of coherence and clarity to our subsequent figures. This chapter was greatly improved by a thorough review by Emmanuel Lellouch.

References

Abernathy, M.R., Tegler, S.C., Grundy, W.M., Licandro, J., Romanishin, W., Cornelison, D., et al., 2009. Digging into the surface of the icy dwarf planet Eris. Icarus 199, 520–525.
Armstrong, G.T., Brickwedde, F.G., Scott, R.B., 1955. Vapor pressures of methane. J. Res. Natl. Bur. Stand. 55 (1), 39–52.
Atkins, P., de Paula, J., 2009. Elements of Physical Chemistry, fifth ed. Oxford University Press, Oxford.
Barucci, M.A., Cruikshank, D.P., Dotto, E., Merlin, F., Poulet, F., Dalle Ore, C.M., et al., 2005. Is Sedna another Triton? Astron. Astrophys. 439, L1–L4.

Barucci, M.A., Merlin, F., Guilbert, A., de Bergh, C., Alvarez-Candal, A., Hainaut, O., et al., 2008. Surface composition and temperature of the TNO Orcus. Astron. Astrophys. 479, L13–L16.

Barucci, M.A., Dalle Ore, C.M., Alvarez-Candal, A., de Bergh, C., Merlin, F., Dumas, C., et al., 2010. (90377) Sedna: investigation of surface compositional variation. Astron. J. 140, 2095–2100.

Barucci, M.A., Dalle Ore, C.M., Perna, D., Cruikshank, D.P., Doressoundiram, A., Alvarez-Candal, A., et al., 2015. (50000) Quaoar: surface composition variability. Astron. Astrophys. 584, A107.

Benedetti-Rossi, G., Sicardy, B., Buie, M.W., Ortiz, J.L., Vieira-Martins, R., Keller, J.M., et al., 2016. Results from the 2014 November 15th multi-chord stellar occultation by the TNO (229762) 2007 UK_{126}. Astron. J. 152, 156.

Benedetti-Rossi, G., Santos-Sanz, P., Ortiz, J.L., Assafin, M., Sicardy, B., Morales, N., et al., 2019. The Trans-Neptunian object (84922) 2003 VS2 through stellar occultations. https://ui.adsabs.harvard.edu/abs/2019arXiv190806645B/abstract.

Bertrand, T., Forget, F., 2016. Observed glacier and volatile distribution on Pluto from atmosphere-topography processes. Nature 540, 86–89.

Bertrand, T., Forget, F., Umurhan, O.M., Grundy, W.M., Schmitt, B., Protopapa, S., et al., 2018. The nitrogen cycles on Pluto over seasonal and astronomical timescales. Icarus 309, 277–296.

Bird, G.A., 1994. Molecular Gas Dynamics and the Direct Simulation of Gas Flows. Clarendon, Oxford.

Borovik, E.S., Grishin, S.F., Grishina, E.Y., 1960. The vapor pressure of nitrogen and hydrogen at low pressures. Sov. Phys. Tech. Phys. (Engl. Transl.) 5 (5), 506–511.

Braga-Ribas, F., Sicardy, B., Ortiz, J.L., Lellouch, E., Tancredi, G., Lecacheux, J., 2013. The size, shape, albedo, density, and atmospheric limit of transneptunian object (50000) Quaoar from multi-chord stellar occultations. Astrophys. J. 773, 26.

Braga-Ribas, F., Sicardy, B., Ortiz, J.L., Snodgrass, C., Roques, F., Vieira-Martins, R., 2014a. A ring system detected around the Centaur (10199) Chariklo. Nature 508, 72–75.

Braga-Ribas, F., Vieira-Martins, R., Assafin, M., Camargo, J.I.B., Sicardy, B., Ortiz, J.L., 2014b. Stellar occultations by transneptunian and centaurs objects: results from more than 10 observed events. Revista Mexicana Astron. Astrofisica Conf. Ser. 44, 3.

Broadfoot, A.L., Atreya, S.K., Bertaux, J.L., Blamont, J.E., Dessler, A.J., Donahue, T.M., et al., 1989. Ultraviolet spectrometer observations of Neptune and Triton. Science 246, 1459–1466.

Brosch, N., 1995. The 1985 stellar occultation by Pluto. Mon. Not. R. Astron. Soc. 276, 571–578.

Brown, M.E., 2008. The largest Kuiper belt objects. In: The Solar System Beyond Neptune. University of Arizona Press, Tucson, AZ, pp. 335–344.

Brown, M.E., 2012. The compositions of Kuiper belt objects. Annu. Rev. Earth Planet. Sci. 40, 467–494.

Brown, R.H., Cruikshank, D.P., Veverka, J., Helfenstein, P., Eluszkiewicz, J., 1995. Surface composition and photometric properties of Triton. In: Cruikshank, D.P. (Ed.), Neptune and Triton. University of Arizona Press, Tucson, AZ, pp. 991–1030.

Brown, M.E., Trujillo, C.A., Rabinowitz, D.L., 2005. Discovery of a planetary-sized object in the scattered Kuiper belt. Astrophys. J. 635, L97–L100.

Brown, M.E., Barkume, K.M., Blake, G.A., Schaller, E.L., Rabinowitz, D.L., Roe, H.G., et al., 2007. Methane and ethane on the bright Kuiper belt object 2005 FY_9. Astron. J. 133, 284–289.

Brown, M.E., Burgasser, A.J., Fraser, W.C., 2011. The surface composition of large Kuiper belt object 2007 OR_{10}. Astrophys. J. 738, L26.

Brown, M.E., Schaller, E.L., Blake, G.A., 2015. Irradiation products on dwarf planet Makemake. Astron. J. 149, 105.

Camargo, J.I.B., Desmars, J., Braga-Ribas, F., Vieira-Martins, R., Assafin, M., Sicardy, B., et al., 2018. The future of stellar occultations by distant solar system bodies: perspectives from the Gaia astrometry and the deep sky surveys. Planet. Space Sci. 154, 59–62.

Carry, B., Hestroffer, D., DeMeo, F.E., Thirouin, A., Berthier, J., Lacerda, P., et al., 2011. Integral-field spectroscopy of (90482) Orcus-Vanth. Astron. Astrophys. 534, A115.

Cruikshank, D.P., Roush, T.L., Owen, T.C., Geballe, T.R., de Bergh, C., Schmitt, B., et al., 1993. Ices on the surface of Triton. Science 261, 742–745.

Cruikshank, D.P., Schmitt, B., Roush, T.L., Owen, T.C., Quirico, E., Geballe, T.R., et al., 2000. Water ice on Triton. Icarus 147, 309–316.

Cruikshank, D.P., Grundy, W.M., DeMeo, F.E., Buie, M.W., Binzel, R.P., Jennings, D.E., et al., 2015. The surface compositions of Pluto and Charon. Icarus 246, 82–92.

Dalle Ore, C.M., Barucci, M.A., Emery, J.P., Cruikshank, D.P., Dalle Ore, L.V., Merlin, F., et al., 2009. Composition of KBO (50000) Quaoar. Astron. Astrophys. 501, 349–357.

Dalle Ore, C.M., Barucci, M.A., Emery, J.P., Cruikshank, D.P., de Bergh, C., Roush, T.L., et al., 2015. The composition of "ultra-red" TNOs and centaurs. Icarus 252, 311–326.

de Bergh, C., Delsanti, A., Tozzi, G.P., Dotto, E., Doressoundiram, A., Barucci, M.A., 2005. The surface of the transneptunian object 90482 Orcus. Astron. Astrophys. 437, 1115–1120.

de Bergh, C., Schaller, E.L., Brown, M.E., Brunetto, R., Cruikshank, D.P., Schmitt, B., 2013. The ices on transneptunian objects and centaurs. Astrophys. Space Sci. Library 356, 107.

Delsanti, A., Merlin, F., Guilbert-Lepoutre, A., Bauer, J., Yang, B., Meech, K.J., 2010. Methane, ammonia, and their irradiation products at the surface of an intermediate-size KBO? A portrait of Plutino (90482) Orcus. Astron. Astrophys. 520, A40.

DeMeo, F.E., Barucci, M.A., Merlin, F., Guilbert-Lepoutre, A., Alvarez-Candal, A., Delsanti, A., et al., 2010. A spectroscopic analysis of Jupiter-coupled object (52872) Okyrhoe, and TNOs (90482) Orcus and (73480) 2002 PN_{34}. Astron. Astrophys. 521, A35.

Dias-Oliveira, A., Sicardy, B., Lellouch, E., Vieira-Martins, R., Assafin, M., Camargo, J.I.B., et al., 2015. Pluto's atmosphere from stellar occultations in 2012 and 2013. Astrophys. J. 811, 53.

Dias-Oliveira, A., Sicardy, B., Ortiz, J.L., Braga-Ribas, F., Leiva, R., Vieira-Martins, R., et al., 2017. Study of the Plutino object (208996) 2003 AZ_{84} from stellar occultations: size, shape, and topographic features. Astron. J. 154, 22.

Dumas, C., Merlin, F., Barucci, M.A., de Bergh, C., Hainault, O., Guilbert, A., Vernazza, P., Doressoundiram, A., 2007. Surface composition of the largest dwarf planet 136199 Eris (2003 UB_{313}). Astron. Astrophys. 471, 331–334.

Elliot, J.L., Kern, S.D., 2003. Pluto's atmosphere and a targeted-occultation search for other bound KBO atmospheres. Earth Moon Planets 92, 375–393.

Elliot, J.L., Olkin, C.B., 1996. Probing planetary atmospheres with stellar occultations. Annu. Rev. Earth Planet. Sci. 24, 89–124.

Elliot, J.L., Young, L.A., 1992. Analysis of stellar occultation data for planetary atmospheres. I—model fitting, with application to Pluto. Astron. J. 103, 991–1015.

Elliot, J.L., Hammel, H.B., Wasserman, L.H., Franz, O.G., McDonald, S.W., Person, M.J., et al., 1998. Global warming on Triton. Nature 393, 765–767.

Elliot, J.L., et al., 2000a. The prediction and observation of the 1997 July 18 stellar occultation by Triton: more evidence for distortion and increasing pressure in Triton's atmosphere. Icarus 148, 347–369.

Elliot, J.L., Strobel, D.F., Zhu, X., Stansberry, J.A., Wasserman, L.H., Franz, O.G., 2000b. Note: The thermal structure of Triton's middle atmosphere. Icarus 143, 425–428.

Elliot, J.L., Ates, A., Babcock, B.A., Bosh, A.S., Buie, M.W., Clancy, K.B., et al., 2003a. The recent expansion of Pluto's atmosphere. Nature 424, 165–168.

Elliot, J.L., Person, M.J., Qu, S., 2003b. Analysis of stellar occultation data. II. Inversion, with application to Pluto and Triton. Astron. J. 126, 1041–1079.

Emery, J.P., Dalle Ore, C.M., Cruikshank, D.P., Fernández, Y.R., Trilling, D.E., Stansberry, J.A., 2007. Ices on (90377) Sedna: confirmation and compositional constraints. Astron. Astrophys. 466, 395–398.

Erwin, J., Tucker, O.J., Johnson, R.E., 2013. Hybrid fluid/kinetic modeling of Pluto's escaping atmosphere. Icarus 226, 375–384.

Forget, F., Bertrand, T., Vangvichith, M., Leconte, J., Millour, E., Lellouch, E., 2017. A post-New Horizons global climate model of Pluto including the N_2, CH_4 and CO cycles. Icarus 287, 54–71.

Fornasier, S., Dotto, E., Barucci, M.A., Barbieri, C., 2004. Water ice on the surface of the large TNO 2004 DW. Astron. Astrophys. 422, L43–L46.

Fray, N., Schmitt, B., 2009. Sublimation of ices of astrophysical interest: a bibliographic review. Planet. Space Sci. 57, 2053–2080.

Frels, W., Smith, D.R., Ashworth, T., 1974. Vapour pressure of nitrogen below the triple point. Cryogenics 14, 3–7.

French, R.G., Gierasch, P.J., 1976. Diffraction calculation of occultation light curves in the presence of an isothermal atmosphere. Astron. J. 81, 445–451.

Giauque, W.F., Clayton, J.O., 1933. The heat capacity and entropy of nitrogen. Heat of vaporization. Vapor pressures of solid and liquid. The reaction $1/2\ N_2 + 1/2\ O_2 = NO$ from spectroscopic data. J. Am. Chem. Soc. 55 (12), 4875–4889.

Gladstone, G.R., 1998. Lyman-α photolysis in the Primitive Solar Nebula. Final Report for NASA Grant NAG5-4290.

Gladstone, G.R., Young, L.A., 2019. New Horizons observations of the atmosphere of Pluto. Annu. Rev. Earth Planet. Sci. 47, 119–140.

Glein, C.R., Waite, J.H., 2018. Primordial N_2 provides a cosmochemical explanation for the existence of Sputnik Planitia, Pluto. Icarus 313, 79–92.

Grasset, O., Castillo-Rogez, J., Guillot, T., Fletcher, L.N., Tosi, F., 2017. Water and volatiles in the outer solar system. Space Sci. Rev. 212, 835–875.

Grundy, W.M., Young, L.A., 2004. Near-infrared spectral monitoring of Triton with IRTF/SpeX I: establishing a baseline for rotational variability. Icarus 172, 455–465.

Grundy, W.M., Young, L.A., Stansberry, J.A., Buie, M.W., Olkin, C.B., Young, E.F., 2010. Near-infrared spectral monitoring of Triton with IRTF/SpeX II: spatial distribution and evolution of ices. Icarus 205, 594–604.

Guilbert, A., Alvarez-Candal, A., Merlin, F., Barucci, M.A., Dumas, C., de Bergh, C., et al., 2009. ESO-large program on TNOs: near-infrared spectroscopy with SINFONI. Icarus 201, 272–283.

Gulbis, A.A.S., Elliot, J.L., Person, M.J., Adams, E.R., Babcock, B.A., Emilio, M., et al., 2006. Charon's radius and atmospheric constraints from observations of a stellar occultation. Nature 439, 48–51.

Hansen, C.J., Paige, D.A., Young, L.A., 2015. Pluto's climate modeled with new observational constraints. Icarus 246, 183–191.

Harris, A.W., 1998. A thermal model for near-Earth asteroids. Icarus 131, 291–301.

Hofgartner, J.D., Buratti, B.J., Hayne, P.O., Young, L.A., 2018. Ongoing resurfacing of KBO Eris by volatile transport in local, collisional, sublimation atmosphere regime. Icarus. https://doi.org/10.1016/j.icarus.2018.10.028.

Holler, B.J., Young, L.A., Grundy, W.M., Olkin, C.B., 2016. On the surface composition of Triton's southern latitudes. Icarus 267, 255–266.

Howard, A.D., Moore, J.M., 2008. Sublimation-driven erosion on Callisto: a landform simulation model test. Geophys. Res. Lett. 35, L03203.

Howard, A.D., Moore, J.M., Schenk, P.M., White, O.L., Spencer, J., 2012. Sublimation-driven erosion on Hyperion: topographic analysis and landform simulation model tests. Icarus 220, 268–276.

Hubbard, W.B., Hunten, D.M., Dieters, S.W., Hill, K.M., Watson, R.D., 1988. Occultation evidence for an atmosphere on Pluto. Nature 336, 452–454.

Ingersoll, A.P., 1990. Dynamics of Triton's atmosphere. Nature 344, 315–317.

Ingersoll, A.P., Summers, M.E., Schlipf, S.G., 1985. Supersonic meteorology of Io—sublimation-driven flow of SO_2. Icarus 64, 375–390.

Jewitt, D.C., Luu, J., 2004. Crystalline water ice on the Kuiper belt object (50000) Quaoar. Nature 432, 731–733.

Johnson, R.E., Volkov, A.N., Erwin, J.T., 2013a. Erratum: "Molecular-kinetic simulations of escape from the ex-planet and exoplanets: criterion for transonic flow". Astrophys. J. 779, L30.

Johnson, R.E., Volkov, A.N., Erwin, J.T., 2013b. Molecular-kinetic simulations of escape from the ex-planet and exoplanets: criterion for transonic flow. Astrophys J. Lett. 768, L4.

Johnson, R.E., Oza, A., Young, L.A., Volkov, A.N., Schmidt, C., 2015. Volatile loss and classification of Kuiper belt objects. Astrophys. J. 809, 43.

Kaye, G.W.C., Laby, T.H., 1973. Tables of Physical and Chemical Constants, fourteenth ed. Longman Scientific & Technical, London.

Lellouch, E., de Bergh, C., Sicardy, B., Ferron, S., Käufl, H.U., 2010. Detection of CO in Triton's atmosphere and the nature of surface-atmosphere interactions. Astron. Astrophys. 512, L8.

Lellouch, E., Santos-Sanz, P., Lacerda, P., Mommert, M., Duffard, R., Ortiz, J.L., et al., 2013. "TNOs are Cool": a survey of the Trans-Neptunian region. IX. Thermal properties of Kuiper belt objects and centaurs from combined Herschel and Spitzer observations. Astron. Astrophys. 557, A60.

Lellouch, E., Gurwell, M., Butler, B., Fouchet, T., Lavvas, P., Strobel, D.F., et al., 2017. Detection of CO and HCN in Pluto's atmosphere with ALMA. Icarus 286, 289–307.

Levi, A., Podolak, M., 2009. Cornoa-like atmospheric escape from KBOs. Icarus 202, 681–693.

Licandro, J., Grundy, W.M., Pinilla-Alonso, N., Leisy, P., 2006a. Visible spectroscopy of 2003 UB_{313}: evidence for N_2 ice on the surface of the largest TNO? Astron. Astrophys. 458, L5–L8.

Licandro, J., Pinilla-Alonso, N., Pedani, M., Oliva, E., Tozzi, G.P., Grundy, W.M., 2006b. The methane ice rich surface of large TNO 2005 FY_9: a Pluto-twin in the Trans-Neptunian belt? Astron. Astrophys. 445, L35–L38.

Lorenzi, V., Pinilla-Alonso, N., Licandro, J., Dalle Ore, C.M., Emery, J.P., 2014. Rotationally resolved spectroscopy of (20000) Varuna in the near-infrared. Astron. Astrophys. 562, A85.

Lorenzi, V., Pinilla-Alonso, N., Licandro, J., 2015. Rotationally resolved spectroscopy of dwarf planet (136472) Makemake. Astron. Astrophys. 577, A86.

Mangold, N., 2011. Ice sublimation as a geomorphic process: a planetary perspective. Geomorphology 126, 1–17.

McKinnon, W.B., Leith, A.C., 1995. Gas drag and the orbital evolution of a captured Triton. Icarus 118, 392–413.

Merlin, F., Alvarez-Candal, A., Delsanti, A., Fornasier, S., Barucci, M.A., DeMeo, F.E., et al., 2009. Stratification of methane ice on Eris' surface. Astron. J. 137, 315–328.

Merlin, F., Lellouch, E., Quirico, E., Schmitt, B., 2018. Triton's surface ices: distribution, temperature and mixing state from VLT/SINFONI observations. Icarus 314, 274–293.

Meza, E., Sicardy, B., Assafin, M., Ortiz, J.L., Bertrand, T., Lellouch, E., et al., 2019. Lower atmosphere and pressure evolution on Pluto from ground-based stellar occultations, 1988–2016. Astron. Astrophys. 625, A42.

Millis, R.L., et al., 1993. Pluto's radius and atmosphere—results from the entire 9 June 1988 occultation data set. Icarus 105, 282.

Moore, J.M., Spencer, J.R., 1990. Koyaanismuuyaw: the hypothesis of a perennially dichotomous Triton. Geophys. Res. Lett. 17, 1757–1760.

Moore, J.M., McKinnon, W.B., Spencer, J.R., Howard, A.D., Schenk, P.M., Beyer, R.A., et al., 2016. The geology of Pluto and Charon through the eyes of New Horizons. Science 351, 1284–1293.

Müller, M., Marchis, F., Emery, J.P., Harris, A.W., Mottola, S., Hestroffer, D., et al., 2010. Eclipsing binary Trojan asteroid Patroclus: thermal inertia from Spitzer observations. Icarus 205, 505–515.

Oliveira, J.M., Sicardy, B., Meza, E., Desmars, J., Lecacheux, J., Assafin, M., et al., 2018. Stellar occultation of Triton on October 5th, 2017. In: European Planetary Science Congress EPSC2018-172.

Olkin, C.B., Elliot, J.L., Hammel, H.B., Cooray, A.R., McDonald, S.W., Foust, J.A., et al., 1997. The thermal structure of Triton's atmosphere: results from the 1993 and 1995 occultations. Icarus 129, 178–201.

Olkin, C.B., Young, L.A., Borncamp, D., Pickles, A., Sicardy, B., Assafin, M., et al., 2015. Evidence that Pluto's atmosphere does not collapse from occultations including the 2013 May 04 event. Icarus 246, 220–225.

Ortiz, J.L., Sicardy, B., Braga-Ribas, F., Alvarez-Candal, A., Lellouch, E., Duffard, R., et al., 2012. Albedo and atmospheric constraints of dwarf planet Makemake from a stellar occultation. Nature 491, 566–569.

Ortiz, J.L., Santos-Sanz, P., Sicardy, B., Benedetti-Rossi, G., Bérard, D., Morales, N., et al., 2017. The size, shape, density and ring of the dwarf planet Haumea from a stellar occultation. Nature 550, 219–223.

Pál, A., Kiss, C., Müller, T.G., Molnár, L., Szabó, R., Szabó, G.M., et al., 2016. Large size and slow rotation of the Trans-Neptunian object (225088) 2007 OR_{10} discovered from Herschel and K2 observations. Astron. J. 151, 117.

Parker, A., Pinilla-Alonso, N., Santos-Sanz, P., Stansberry, J., Alvarez-Candal, A., Bannister, M., et al., 2016. Physical characterization of TNOs with the James Webb Space Telescope. Publ. Astron. Soc. Pac. 128, 018010.

Pasachoff, J.M., Babcock, B.A., Durst, R.F., Seeger, C.H., Levine, S.E., Bosh, A.S., et al., 2017. Pluto occultation on 2015 June 29 UTC with central flash and atmospheric spikes just before the New Horizons flyby. Icarus 296, 305–314.

Perna, D., Hromakina, T., Merlin, F., Ieva, S., Fornasier, S., Belskaya, I., et al., 2017. The very homogeneous surface of the dwarf planet Makemake. Mon. Not. R. Astron. Soc. 466, 3594–3599.

Person, M.J., Schindler, K., Bosh, A.S., Wolf, J., Levine, S.E., Zuluaga, C.A., et al., 2018. Airborne and ground observations of the stellar occultation by Triton on 5 October 2017. In: AAS/Division for Planetary Sciences Meeting Abstracts No. 416, 10.

Protopapa, S., Grundy, W.M., Tegler, S.C., Bergonio, J.M., 2015. Absorption coefficients of the methane-nitrogen binary ice system: implications for Pluto. Icarus 253, 179–188.

Protopapa, S., Grundy, W.M., Reuter, D.C., Hamilton, D.P., Dalle Ore, C.M., Cook, J.C., et al., 2017. Pluto's global surface composition through pixel-by-pixel Hapke modeling of New Horizons Ralph/LEISA data. Icarus 287, 218–228.

Quirico, E., Schmitt, B., 1997. Near-infrared spectroscopy of simple hydrocarbons and carbon oxides diluted in solid N_2 and as pure ices: implications for Triton and Pluto. Icarus 127, 354–378.

Quirico, E., Douté, S., Schmitt, B., de Bergh, C., Cruikshank, D.P., Owen, T.C., et al., 1999. Composition, physical state, and distribution of ices at the surface of Triton. Icarus 139, 159–178.

Rubin, M., Altwegg, K., Balsiger, H., Bar-Nun, A., Berthelier, J.-J., Bieler, A., et al., 2015. Molecular nitrogen in comet 67P/Churyumov-Gerasimenko indicates a low formation temperature. Science 348, 232–235.

Santos-Sanz, P., 2017. Physical characterization of Kuiper belt objects from stellar occultations and thermal measurements. In: European Planetary Science Congress 11, EPSC2017-97.

Santos-Sanz, P., French, R.G., Pinilla-Alonso, N., Stansberry, J., Lin, Z.-Y., Zhang, Z.-W., et al., 2016. James Webb Space Telescope observations of stellar occultations by solar system bodies and rings. Publ. Astron. Soc. Pac. 128, 018011.

Schaller, E.L., Brown, M.E., 2007a. Volatile loss and retention on Kuiper belt objects. Astrophys. J. 659, L61–L64.
Schaller, E.L., Brown, M.E., 2007b. Detection of methane on Kuiper belt object (50000) Quaoar. Astrophys. J. 670, L49–L51.
Schmitt, Philippe, S., Grundy, W.M., Reuter, D.C., Côte, R., Quirico, E., et al., 2017. Physical state and distribution of materials at the surface of Pluto from New Horizons LEISA imaging spectrometer. Icarus 287, 229–260.
Shinoda, T., 1969. Vapor pressure of carbon monoxide in condensed phases. Bull. Chem. Soc. Jpn 42, 1815–1820.
Sicardy, B., Ferri, F., Roques, F., Lecacheux, J., Pau, S., Brosch, N., et al., 1999. The structure of Titan's stratosphere from the 28 SGR occultation. Icarus 142, 357–390.
Sicardy, B., Widemann, T., Lellouch, E., Veillet, C., Cuillandre, J.-C., Colas, F., et al., 2003. Large changes in Pluto's atmosphere as revealed by recent stellar occultations. Nature 424, 168–170.
Sicardy, B., Colas, F., Maquet, L., Vachier, F., Doressoundiram, A., Roques, F., et al., 2010. The 2010, February 19 stellar occultation by Varuna. Bull. Am. Astron. Soc. 42, 23.11.
Sicardy, B., Ortiz, J.L., Assafin, M., Jehin, E., Maury, A., Lellouch, E., et al., 2011. A Pluto-like radius and a high albedo for the dwarf planet Eris from an occultation. Nature 478, 493–496.
Sicardy, B., Talbot, J., Meza, E., Camargo, J.I.B., Desmars, J., Gault, D., et al., 2016. Pluto's atmosphere from the 2015 June 29 ground-based stellar occultation at the time of the new Horizons Flyby. Astrophys. J. 819, L38.
Spencer, J.R., 1990. A rough-surface thermophysical model for airless planets. Icarus 83, 27–38.
Spencer, J.R., Stansberry, J.A., Trafton, L.M., Young, E.F., Binzel, R.P., Croft, S.K., 1997. Volatile transport, seasonal cycles, and atmospheric dynamics on Pluto. In: In: Pluto and Charon. University of Arizona Press, Tucson, AZ, pp. 435–473.
Stern, S.A., Trafton, L.M., 2008. On the atmospheres of objects in the Kuiper belt. In: The Solar System Beyond Neptune. University of Arizona Press, Tucson, AZ, pp. 365–380.
Stern, S.A., Kammer, J.A., Gladstone, G.R., Steffl, A.J., Cheng, A.F., Young, L.A., et al., 2017. New Horizons constraints on Charon's present day atmosphere. Icarus 287, 124–130.
Tan, S.P., Kargel, J.S., 2018. Solid-phase equilibria on Pluto's surface. Mon. Not. R. Astron. Soc. 474, 4254–4263.
Tegler, S.C., Grundy, W.M., Romanishin, W., Consolmagno, G.J., Mogren, K., Vilas, F., 2007. Optical spectroscopy of the large Kuiper belt objects 136472 (2005 FY9) and 136108 (2003 EL61). Astron. J. 133, 526–530.
Tegler, S.C., Grundy, W.M., Vilas, F., Romanishin, W., Cornelison, D.M., Consolmagno, G.J., 2008. Evidence of N_2-ice on the surface of the icy dwarf planet 136472 (2005 FY9). Icarus 195, 844–850.
Tegler, S.C., Grundy, W.M., Olkin, C.B., Young, L.A., Romanishin, W., Cornelison, D.M., et al., 2012. Ice mineralogy across and into the surfaces of Pluto, Triton, and Eris. Astrophys. J. 751, 76.
Tickner, A.W., Lossing, F.P., 1951. The measurement of low vapor pressures by means of a mass spectrometer. J. Phys. Chem. 55 (5), 733–740.
Toigo, A.D., Gierasch, P.J., Sicardy, B., Lellouch, E., 2010. Thermal tides on Pluto. Icarus 208, 402–411.
Trafton, L.M., 1984. Large seasonal variations in Triton's atmosphere. Icarus 58, 312–324.
Trafton, L.M., 2015. On the state of methane and nitrogen ice on Pluto and Triton: implications of the binary phase diagram. Icarus 246, 197–205.
Trafton, L.M., Matson, D.L., Stansberry, J.A., 1998. Surface/atmosphere interactions and volatile transport (Triton, Pluto and Io). In: Solar System Ices. Kluwer Academic Publishers, Dordrecht. p. 773.
Trujillo, C.A., Brown, M.E., Rabinowitz, D.L., Geballe, T.R., 2005. Near-infrared surface properties of the two intrinsically brightest minor planets: (90377) Sedna and (90482) Orcus. Astrophys. J. 627, 1057–1065.
Trujillo, C.A., Sheppard, S.S., Schaller, E.L., 2011. A photometric system for detection of water and methane ices on Kuiper belt objects. Astrophys. J. 730, 105.
Tucker, O.J., Erwin, J.T., Deighan, J.I., Volkov, A.N., Johnson, R.E., 2012. Thermally driven escape from Pluto's atmosphere: a combined fluid/kinetic model. Icarus 217, 408–415.
Volkov, A.N., Johnson, R.E., Tucker, O.J., Erwin, J.T., 2011a. Thermally driven atmospheric escape: transition from hydrodynamic to jeans escape. Astrophys. J. 729, L24.
Volkov, A.N., Tucker, O.J., Erwin, J.T., Johnson, R.E., 2011b. Kinetic simulations of thermal escape from a single component atmosphere. Phys. Fluids 23, 066601-16.
Walker, A.C., Moore, C.H., Goldstein, D.B., Varghese, P.L., Trafton, L.M., 2012. A parametric study of Io's thermophysical surface properties and subsequent numerical atmospheric simulations based on the best fit parameters. Icarus 220, 225–253.
Wong, M.C., Smyth, W.H., 2000. Model calculations for Io's atmosphere at eastern and western elongations. Icarus 146, 60–74.

Yelle, R.V., Lunine, J.I., 1989. Evidence for a molecule heavier than methane in the atmosphere of Pluto. Nature 339, 288–290.

Yelle, R.V., Lunine, J.I., Pollack, J.B., Brown, R.H., 1995. Lower atmospheric structure and surface-atmosphere interactions on Triton. In: Neptune and Triton. University of Arizona Press, Tucson, AZ, pp. 1031–1105.

Young, E.F., 1993. An Albedo Map and Frost Model of Pluto (Ph.D. thesis). Massachusetts Institute of Technology.

Young, L.A., 2012. Volatile transport on inhomogeneous surfaces: I—analytic expressions, with application to Pluto's day. Icarus 221, 80–88.

Young, L.A., 2013. Pluto's seasons: new predictions for New Horizons. Astrophys. J. 766, L22.

Young, L.A., 2017. Volatile transport on inhomogeneous surfaces: II. Numerical calculations (VT3D). Icarus 284, 443–476.

Young, L., McKinnon, W.B.. 2013. Atmospheres on volatile-bearing Kuiper belt objects. In: AAS/Division for Planetary Sciences Meeting Abstracts No. 45, ID507.02.

Young, E.F., French, R.G., Young, L.A., Ruhland, C.R., Buie, M.W., Olkin, C.B., et al., 2008. Vertical structure in Pluto's atmosphere from the 2006 June 12 stellar occultation. Astron. J. 136, 1757–1769.

Young, L.A., Stark, G., Vervack, R.J., 2002. Triton's atmosphere in 1989: new lab data, new profiles. In AAS/Division for Planetary Sciences Meeting Abstracts No. 34, ID21.04.

Young, L.A., Kammer, J.A., Steffl, A.J., Gladstone, G.R., Summers, M.E., Strobel, D.F., et al., 2018. Structure and composition of Pluto's atmosphere from the New Horizons solar ultraviolet occultation. Icarus 300, 174–199.

Zhang, X., Strobel, D.F., Imanaka, H., 2017. Haze heats Pluto's atmosphere yet explains its cold temperature. Nature 551, 352–355.

Zhu, X., Strobel, D.F., Erwin, J.T., 2014. The density and thermal structure of Pluto's atmosphere and associated escape processes and rates. Icarus 228, 301–314.

This page intentionally left blank